A study of the direct and indirect effects of aerosols using global satellite data sets of aerosol and cloud parameters

Miho Sekiguchi,[1] Teruyuki Nakajima,[1] Kentaroh Suzuki,[1] Kazuaki Kawamoto,[2] Akiko Higurashi,[3] Daniel Rosenfeld,[4] Itaru Sano,[5] and Sonoyo Mukai[5]

Received 26 December 2002; revised 8 May 2003; accepted 20 May 2003; published 21 November 2003.

[1] The present study investigated the correlations between aerosol and cloud parameters derived from satellite remote sensing for evaluating the radiative forcing of the aerosol indirect effect. The global statistics showed that the effective particle radius and the optical thickness of low clouds correlate well with the column number concentration of the aerosol particles, indicating an aerosol indirect effect. A correlation of the cloud fraction with the aerosol number was also seen, whereas we could not find a significant correlation of the cloud-top temperature with the column aerosol number. Furthermore, the regional statistics presented that positive correlations between the cloud optical thickness and cloud fraction with the aerosol column number concentration exist in most regions consistent with the global mean statistics. However, the effective cloud particle radius showed a tendency similar to the global correlation only around the seashore regions. Using these correlations and assuming that the aerosol column number concentration has increased by 30% from the preindustrial era, the total radiative forcing of the aerosol indirect effect was evaluated to be about -0.6 to -1.2 W m^{-2}. The radiative forcing of the aerosol direct effect from the satellite-retrieved parameters was also evaluated as -0.4 W m^{-2} over the ocean. The cloud-top temperature was found to be insensitive to the change in the aerosol number, although there was a distinct negative correlation between the aerosol number and cloud temperature at which the cloud particle grows to a radius of 14 μm. This particular dependency of the cloud temperature suggests that aerosols acts on clouds so as to change cloud particle size near the cloud top, optical thickness, and fraction but to keep their cloud-top temperature without causing a significant longwave radiative forcing. *INDEX TERMS:* 0305 Atmospheric Composition and Structure: Aerosols and particles (0345, 4801); 0320 Atmospheric Composition and Structure: Cloud physics and chemistry; 3359 Meteorology and Atmospheric Dynamics: Radiative processes; 3360 Meteorology and Atmospheric Dynamics: Remote sensing; *KEYWORDS:* aerosol, radiative forcing, indirect effect

Citation: Sekiguchi, M., T. Nakajima, K. Suzuki, K. Kawamoto, A. Higurashi, D. Rosenfeld, I. Sano, and S. Mukai, A study of the direct and indirect effects of aerosols using global satellite data sets of aerosol and cloud parameters, *J. Geophys. Res.*, *108*(D22), 4699, doi:10.1029/2002JD003359, 2003.

1. Introduction

[2] With the advance of human activity, anthropogenic aerosols have increased since the preindustrial era similarly to carbon dioxide and may have had a significant influence on Earth's climate. It has been recognized that the aerosol direct effect caused by scattering and absorbing radiation may offset part of the greenhouse warming, but it is difficult to precisely determine the effect because of complexities in the aerosol transport process and in the chemical and optical properties of the aerosols. They also cause an indirect effect by modifying the cloud microphysics, but the magnitude of the radiative forcing of this effect is uncertain [*Intergovernmental Panel on Climate Change* (*IPCC*), 2001] because the cloud modification process is highly variable and complicated.

[3] It is thought that there are two kinds of indirect effects. The first indirect effect is that increasing aerosols cause an increase in the droplet number concentration and a decrease in the droplet size with a fixed liquid water content (LWC) [*Twomey*, 1974]. This effect may cause an increase in the cloud reflectivity and contribute to a cooling of Earth. The second indirect effect, also known as the cloud lifetime effect, is that the reduction in the cloud droplet size affects the precipitation efficiency causing a significant increase in LWC and the cloud lifetime [*Albrecht*, 1989]. This effect may cause a further increase in the global albedo. Several researchers tried to estimate the indirect radiative forcing using empirical relationships between the sulfate aerosol

[1]Center for Climate System Research, University of Tokyo, Tokyo, Japan.
[2]Research Institute for Humanity and Nature, Kyoto, Japan.
[3]National Institutes for Environmental Studies, Ibaraki, Japan.
[4]Hebrew University of Jerusalem, Jerusalem, Israel.
[5]Faculty of Science and Technology, Kinki University, Osaka, Japan.

0148-0227/03/2002JD003359$09.00

and the cloud droplet number concentration [*Jones et al.*, 1994; *Jones and Slingo*, 1996; *Lohmann and Feichter*, 1997], and parameterizations of the cloud nucleation process [*Lohmann et al.*, 2000] in different GCMs. However, their studies significantly disagree among them, both on the estimated values and on the distributions. Reviewing these values, *IPCC* [2001] concluded that the radiative forcing of the first indirect effect exists over a rather wide range from 0 to -2 W m^{-2}. *IPCC* [2001] did not give any estimate for the second indirect effect because there are few studies to confirm the estimation.

[4] Satellites have been also used to observe cloud modifications by aerosols. *Kaufman and Nakajima* [1993] and *Kaufman and Fraser* [1997] observed that clouds were affected by biomass burning over the Amazon Basin, and they showed evidence for two types of cloud modification due to biomass burning aerosols. *Han et al.* [1998] found that the cloud albedo increases with decreasing droplet size for optically thicker clouds, but contrary for thinner clouds, because the liquid water content may not remain constant if the cloud droplet number concentration changes. *Wetzel and Stowe* [1999] and *Nakajima et al.* [2001] showed the correlation between cloud and aerosol microphysical parameters using AVHRR satellite data. The latter has estimated the first and second indirect radiative forcing ranges from -0.7 to -1.7 W m^{-2} over the global ocean using their correlation and with an assumption of 15% to 40% increase in the aerosol number after the industrial revolution.

[5] Along with the progress in understanding the radiative forcing of the aerosol indirect effect, the aerosol effect on the hydrological cycle, through modification of the vertical thickness and horizontal extent of clouds, has recently received much attention. *Albrecht* [1989] studied the cloud fraction change using a one-dimensional model and suggested that the precipitation efficiency of shallow clouds decreases and the cloud fraction increases. *Pincus and Baker* [1994] showed that increasing LWC might change the cloud geometrical thickness using a simple model of stratocumulus clouds in the marine boundary layer. This effect is possible to change the radiation budget and decrease the outgoing longwave radiation. *Rosenfeld* [2000] demonstrated using TRMM data that urban and industrial air pollution could reduce the cloud particle size and suppress precipitation. Furthermore, *Ramanathan et al.* [2001] proposed that the reduction in the surface solar radiation due to anthropogenic aerosols over the Indian Ocean is balanced by a reduction in the evaporation, which will have to be balanced by a reduction in rainfall and effectively spin down the hydrological cycle. However, *Ackerman et al.* [2000] observed that the cloud fraction might be reduced by solar radiation absorption of soot particles.

[6] In this study, we perform a comprehensive investigation of the correlation between cloud parameters and the column aerosol number by extending the method of *Nakajima et al.* [2001]. In this statistical method, we pay attention not only to the microphysical change (effective radius and optical thickness) but also to the cloud structure (cloud height and cloud fraction) modification by aerosols. We further evaluate the radiative forcings of the direct and indirect effects of aerosols using the obtained statistics.

[7] The next section briefly describes the data sets and the radiation code used in calculation of the radiative forcing, and section 3 presents the correlation between the aerosol number concentration and cloud parameters and discusses its significance. Section 4 shows estimations of direct and indirect forcings of aerosols using the derived correlation. Discussions and conclusions follow in section 5.

2. Data Sources and Model Description

2.1. Satellite Data

[8] Two satellite data sets are used in this study. One consists of aerosol and cloud parameters obtained from the National Oceanic and Atmospheric Administration Advanced Very High Resolution Radiometer (NOAA/AVHRR). Data from 60°N to 60°S with a resolution of a 0.5° × 0.5° longitude-latitude box were processed everyday in January, April, July, and October of 1990. The other data set is obtained from Polarization and Directionality of the Earth's Reflectance (POLDER) aboard the Advanced Earth Observing Satellite (ADEOS), which is available over land and ocean. The analyzed region is from 90°N to 90°S with a 0.5° × 0.5° longitude-latitude resolution for every month from November 1996 to June 1997.

[9] The aerosol optical thickness, τ_a, at a reference wavelength of 0.5 μm, and wavelength-mean Ångström exponent, α, were obtained by analysis of the channel-1 and 2 of AVHRR with the algorism developed by *Higurashi and Nakajima* [1999] and *Higurashi et al.* [2000]. They assumed a bimodal lognormal volume spectrum for the aerosol size distribution as

$$\frac{dV}{d\ln r} = \sum_{n=1}^{2} C_n \exp\left[-\frac{1}{2}\left(\frac{\ln r - \ln r_{mn}}{\ln s_n}\right)^2\right], \qquad (1)$$

where V is the volume, r is the particle radius and subscript n indicates the mode number. They adopted r_{m1} = 0.17 μm, r_{m2} = 3.44 μm, s_1 = 1.96 and s_2 = 2.37 for the parameters of the modeled volume spectrum in their retrieval scheme. Two undetermined parameters in equation (1), C_1 and C_2, and hence the optical thickness τ_a and Ångström exponent α can be determined from the two-channel satellite radiances. The wavelength-averaged τ_a and α are calculated by a regression line fitted in the range from 0.36 to 1.05 μm. We calculated the column aerosol number concentration using these retrieved aerosol parameters.

[10] We also used a global distribution of cloud microphysical parameters obtained by analysis of channel-1 (visible), 3 (middle infrared) and 4 (thermal infrared) of AVHRR with the algorithm developed by *Nakajima and Nakajima* [1995] and *Kawamoto et al.* [2001]. This algorithm is applied only to water clouds, so that we limited our analysis to cloudy pixels with the cloud-top temperature greater than 257 K. This threshold is lower than the temperature to perfectly exclude ice particles, so that this data may include ice particles. However, this ice particle contamination will be small because several test analyses with a threshold of 273 K showed no significant difference from the results with 257 K. The analyzed cloud parameters are the effective radius, cloud optical thickness, cloud-top

temperature and cloud fraction. The effective radius is defined as

$$r_e = \frac{\langle r^3 \rangle}{\langle r^2 \rangle} = \frac{\int r^3 n(r) dr}{\int r^2 n(r) dr}, \quad (2)$$

where r is the radius of the cloud droplet, and $n(r)$ is the cloud droplet number per atmospheric column at r. The cloud liquid water content (LWC) can be expressed as:

$$W = LWC \times h = \frac{4}{3}\pi\rho_w \int_0^\infty r^3 n(r) dr = \frac{4}{3}\pi\rho_w N_c r_{v,a}^3, \quad (3)$$

where W is the liquid water path, h is the cloud geometrical thickness, $r_{v,a}$ is the volume-averaged radius, and ρ_w is the density of water. The cloud optical thickness is expressed as:

$$\tau_c = \frac{3}{4}\frac{Q_{ext} W}{r_e}, \quad (4)$$

where Q_{ext} is the extinction efficiency, which is about two for wavelengths much shorter than r_e. We assume a monomodal lognormal number distribution. The cloud amount data are derived from the number of cloudy pixels in each 0.5° × 0.5° segmented box. The temporal and spatial resolution of the data are as same as those of the aerosol data.

[11] The aerosol parameters over the ocean and land are also derived from POLDER data using the combined 2-channel method and a polarimetry method [*Mukai and Sano*, 1999; *Sano and Mukai*, 2000]. The effective cloud particle radius has been retrieved using the angular pattern of the polarized radiance at 0.865 μm [*Yasumoto et al.*, 2002].

2.2. Radiative Transfer Model

[12] We use the radiation code *mstrn8* that is used in the CCSR/NIES AGCM for calculating the radiative forcing. The code combines a *k*-distribution method with the discrete-ordinate method/adding method [*Nakajima et al.*, 2000]. We use an 18-band and 37-channel version with wavelengths that range from 0.2 μm to 200 μm. This code can treat Rayleigh scattering and absorption/emission for gaseous matter and Mie scattering and absorption/emission for particulate matter. The optical properties of aerosols and clouds are assumed to be same as the satellite-retrieved values. We calculate the radiative forcing of aerosols and clouds with the horizontal spatial resolution of 2.5°× 2.5° longitude-latitude grids and 17 vertical levels. The cloud layer is assumed as a single layer because we have only the satellite-derived cloud fraction data. The atmospheric temperature and water vapor profiles are obtained from the ECMWF (European Centre of Medium-Range Weather Forecasts) reanalysis data set for every day of the analysis period. The CO_2 concentration is assumed to be 358.6 ppmv. The O_3 column concentration is adopted from the ISCCP (International Satellite Cloud Climatology Project) data set [*Rossow and Schiffer*, 1999]. The other gaseous concentrations are assumed as those of the U.S. standard atmosphere.

3. Results

[13] In order to evaluate the quantitative magnitude of the aerosol and cloud interaction, we study the correlations between the column number concentration of aerosol particles (N_a) and cloud parameters, i.e., effective radius (r_e), cloud optical thickness (τ_χ), cloud-top temperature (T_c) and cloud fraction (n), which are retrieved from the satellite radiance data, and liquid water path (W), cloud droplet number concentration (N_c) and cloud geometrical thickness (z_h), which are calculated using the satellite-derived cloud parameters. At first, we consider the relation between the aerosol column number concentration and the cloud droplet number concentration, for which the following approximation is considered to be well established [*Twomey*, 1984; *Kaufman and Fraser*, 1997; *Nakajima et al.*, 2001]:

$$\Delta \log_{10} N_c = g \Delta \log_{10} N_a. \quad (5)$$

where g should be less than 1. Using this assumption, equation (3) yields

$$\Delta \log_{10} W = g \Delta \log_{10} N_a + 3 \Delta \log_{10} r_e. \quad (6)$$

If the liquid water path does not significantly change, the relation between N_a and r_e can be expressed as follows:

$$\Delta \log_{10} r_e = g/3 \Delta \log_{10} N_a. \quad (7)$$

Similar to these equations, the relation between N_a and τ_c can be expressed using equations (4) and (6).

$$\Delta \log_{10} W = \Delta \log_{10} \tau_c + \Delta \log_{10} r_e = g \Delta \log_{10} N_a + 3 \Delta \log_{10} r_e \quad (8)$$

If the liquid water path does not significantly change, the following relation is established:

$$\Delta \log_{10} \tau_c = -g/3 \Delta \log_{10} N_a. \quad (9)$$

These equations suggest that we should study the correlations in the form of

$$\log_{10} Y = a_y + b_y \log_{10} N_a. \quad (10)$$

3.1. Global Correlation Between Aerosol and Cloud Parameters

[14] At first, we take the correlation using the spatially and temporally averaged data to find a common feature of the correlation statistics. The AVHRR-derived parameters are averaged spatially over a 2.5° × 2.5° segmented area, and temporally over 3 days, one week, 10 days, 2 weeks and one month from the daily 0.5° × 0.5° data. The averaged values are further used to calculate the correlation line applying a log linear regression method with equation (10). Since there is a large variability in the averaged values, we bin the averaged data into number bins of $\Delta\log_{10}N_a$ =

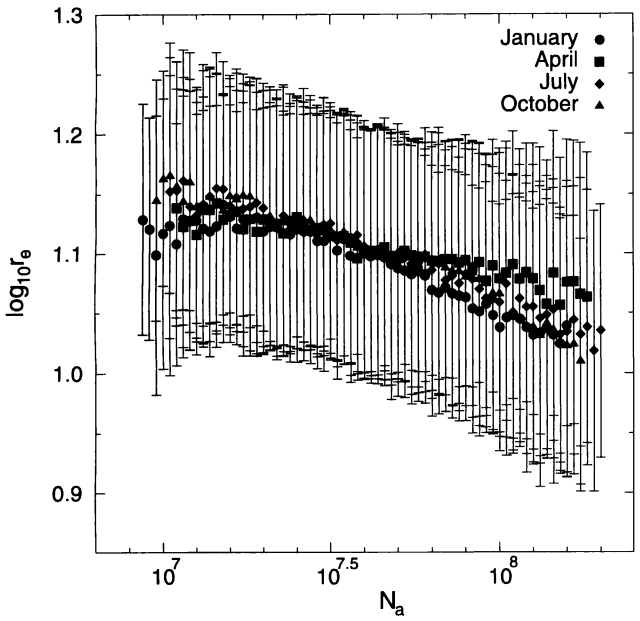

Figure 1. Correlation plots between column aerosol number and cloud effective radius using 2.5° × 2.5° daily averaged AVHRR data. Circles, squares, diamonds, and triangles show averaged values in January, April, July, and October 1990, respectively, and error bars indicate one standard deviation.

0.02 to calculate the mean value and standard deviation in each bin. To select significant data, we do not use the data smaller than the 2.5th percentile or greater than the 97.5th percentile. Figure 1 shows the correlation between $\log_{10}N_a$ and $\log_{10}r_e$ using the 2.5° × 2.5° daily averaged data. Note that the effective cloud particle radius decreases almost linearly with increasing aerosol particle numbers. This tendency is consistent with equation (7) under the assumption of a fixed liquid water path or the first kind indirect effect proposed by *Twomey* [1974]. Using a *t* test, the negative correlation is found to be statistically significant with the 95% significance level for each month. A small correlation slope b_r in magnitude for the turbid conditions of $\log_{10}N_a > 8.0$ indicates a saturation in the cloud response to the large CCN loading as also reported by several researchers [*Leaitch et al.*, 1992; *Martin et al.*, 1994; *Boucher and Lohmann*, 1995; *Nakajima et al.*, 2001]. Figure 2 shows the slopes and coefficients of correlation between $\log_{10}N_a$ and $\log_{10}r_e$ using several spatial and temporal averagings of the original daily 0.5° × 0.5° AVHRR data. It is found that the correlation coefficient approaches one quickly with wider spatial and/or temporary averages and the daily 0.5° × 0.5° data do not look suitable for obtaining a reliable correlation, because of the large variability in the data caused by the decreased number of cases with both cloudy and clear pixels for analysis and also by perturbations of small-scaled dynamical effects. The correlation slope becomes consistently similar values independent of the averaging method with wider spatial and/or temporary averages, though there is a decreasing trend with increasing averaging time. Figure 3 shows the correlation between $\log_{10}N_a$ and $\log_{10}r_e$ using the 2.5° × 2.5° three monthly averaged data (DJF: December 1996 to February 1997; MAM: March to May 1997) derived from POLDER. The figure shows there is an overall consistency between the AVHRR and POLDER data sets over the ocean. Over the ocean, the slope of the POLDER is 2/3 of that of AVHRR, and the correlation slope over land is about half of that over the ocean (Table 1). This land/ocean contrast also indicates a CCN saturation phenomenon in the cloud particle change due to a high CCN loading. Unlike the AVHRR data case, however, the POLDER data show a reduction in the effective radius for very small aerosol numbers for $\log_{10}N_a < 7.4$.

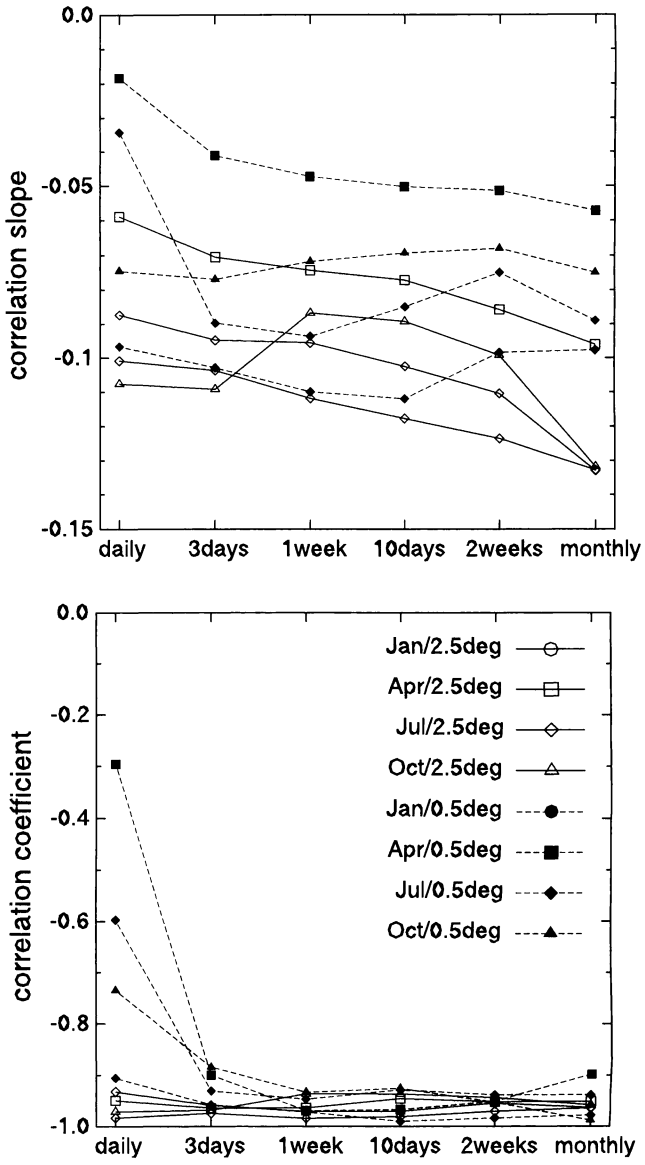

Figure 2. Correlation slopes and coefficients between aerosol column number concentration and cloud effective radius using spatially and temporally averaged data. *X* axis indicates the length of temporal average of the daily 0.5° × 0.5° data. Circles, squares, diamonds, and triangles show averaged values in January, April, July, and October 1990, respectively. Solid and broken lines indicate 2.5° × 2.5° averaged and 0.5° × 0.5° data, respectively.

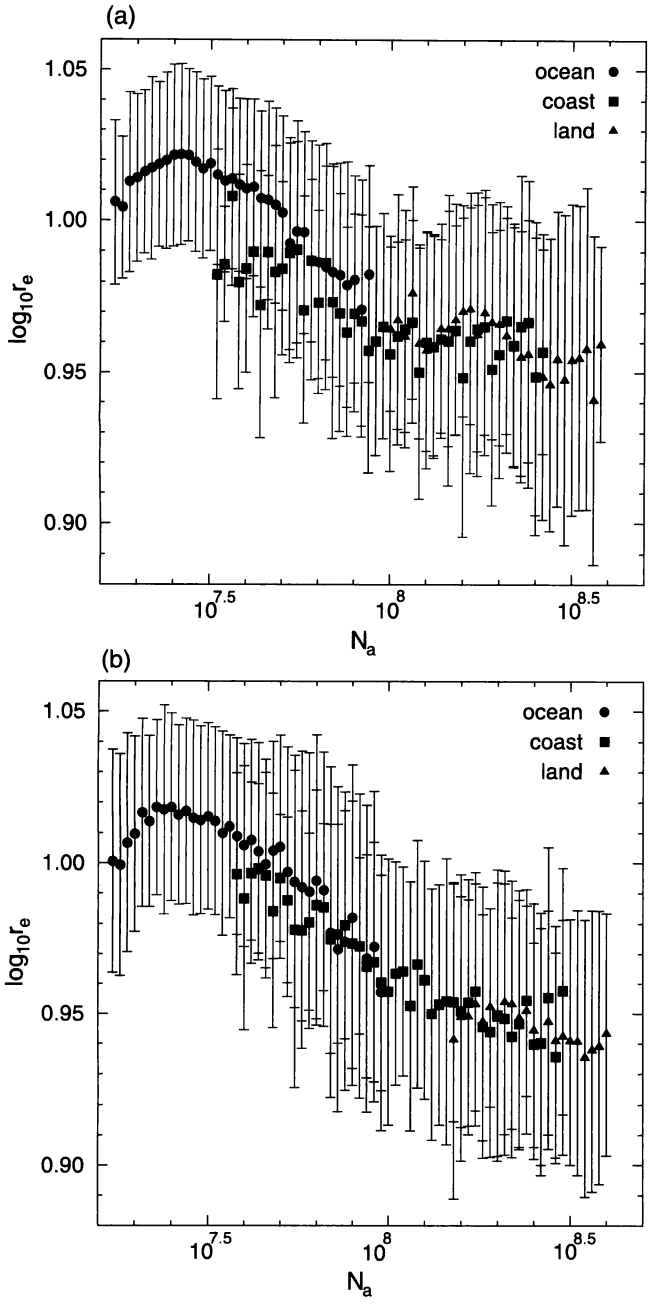

Figure 3. Correlation plots between column aerosol number concentration and cloud effective radius using 2.5° × 2.5° monthly averaged POLDER data. Circles, squares, and diamonds indicate averaged values from (a) December 1996 to February 1997 and from (b) March to May 1997 in each bin over the ocean, seashore, and land, respectively, and error bars indicate one standard deviation.

[15] Figure 4 shows a similar plot between $\log_{10}N_a$ and $\log_{10}\tau_c$. The effect of changing radii and cloud lifetime, referred to as the first and second indirect effects, seems to cause a change in the cloud optical thickness as suggested by the positive correlation in Figure 4. A t test confirmed the existence of the positive correlation as statistically significant of the 95% significance level. Though *Nakajima et al.* [2001] found these correlations in the range of

Table 1. Annual Mean of the Correlation Slopes

Parameter	Global[a]	Regional[b]
	$log_{10}r_e$	
AVHRR	−0.100 ± 0.019	−0.031 ± 0.101
POLDER		
Ocean	−0.0689	−0.0087 ± 0.039
Coastal	−0.0498	−0.022 ± 0.074
Land	−0.0346	−0.0055 ± 0.120
$\log_{10}\tau_c$	0.156 ± 0.046	0.124 ± 0.167
$\log_{10}W$	0.0400 ± 0.0415	
$\log_{10}N_c$	0.388 ± 0.175	
T_c	1.09 ± 2.96	0.767 ± 2.830
T_{14}	−11.97 ± 4.12	
n	0.0857 ± 0.0253	0.115 ± 0.121
z_b	24.0 ± 455	

[a]The average of the global correlation slopes using 2.5° × 2.5° data.
[b]The global average of the regional correlation slopes.

$\log_{10}N_a > 7.8$, the present analysis shows a positive correlation in all the regions shown in the figure. It should be noted, however, that the regression slope in the present study becomes steep around $\log_{10}N_a = 7.8$ to indicate there is a different cloud response with low and high CCN concentrations. This difference may come from the difference in the averaging procedures in the studies, especially with shorter temporal period for averaging (one day in the present case) for retrieving the cloud-aerosol interaction signature more suitably than in the case of one month in the work of *Nakajima et al.* [2001]. Figure 5 shows the slopes and coefficients of correlation between $\log_{10}N_a$ and $\log_{10}\tau_c$ with several spatial and temporal averagings. The correlation parameters significantly depend on the spatial and temporal average methods contrary to the behavior of the correlation parameters for r_e as shown in Figure 2. The April correlation even changes sign from positive to nega-

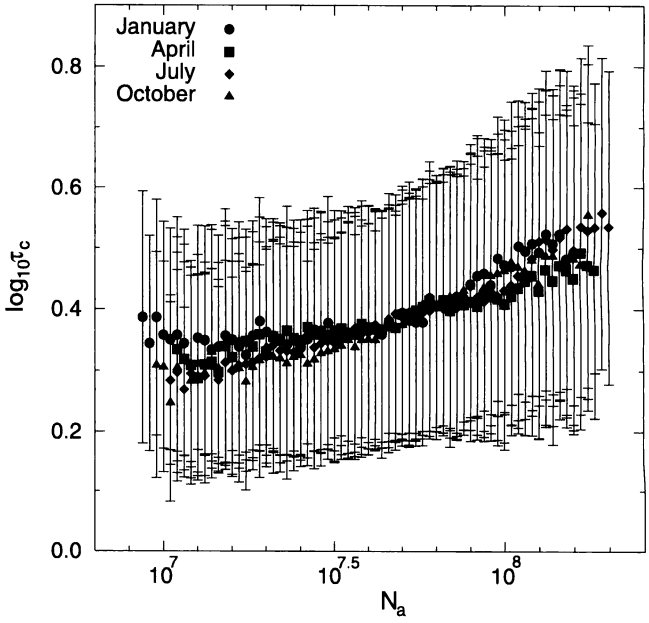

Figure 4. Same as Figure 1, but for the correlation between column aerosol number concentration and cloud optical thickness using 2.5° × 2.5° daily averaged AVHRR data.

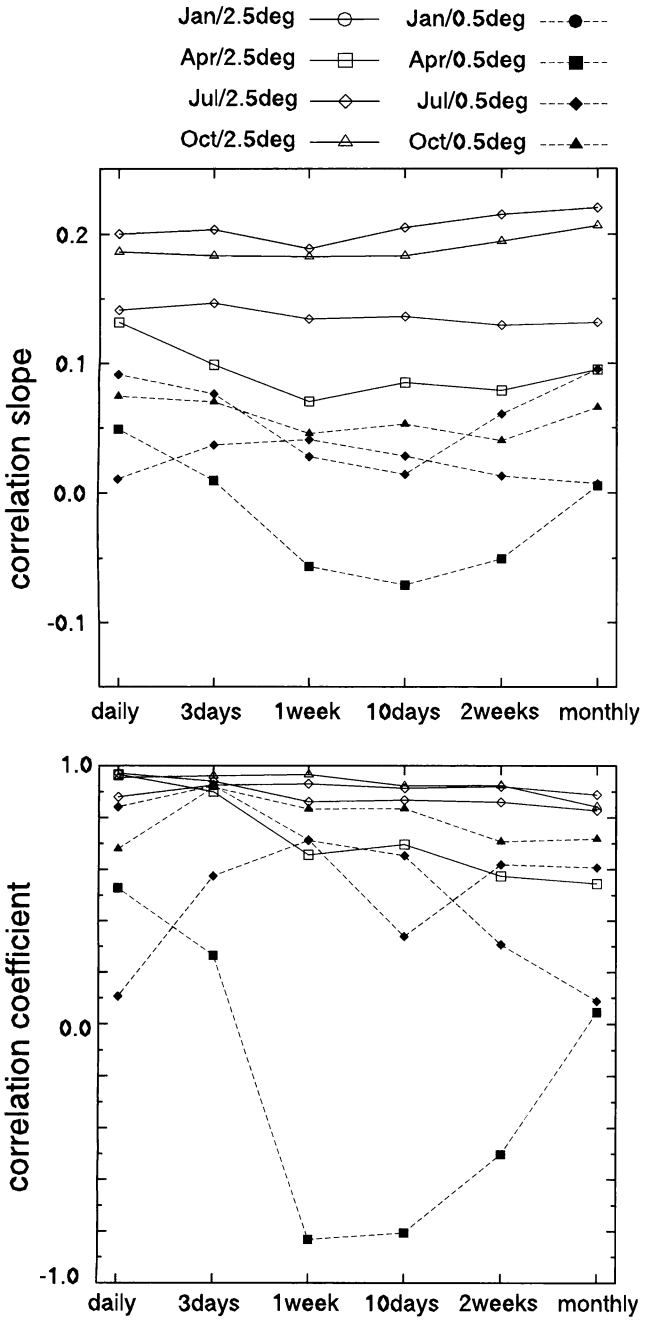

Figure 5. Same as Figure 2, but for the correlation between aerosol column number concentration and cloud optical thickness.

tive with a longer averaging period when the 0.5° × 0.5° data are used. Spatial averaging looks more effective to increase the magnitude of the correlation coefficient and the 2.5° × 2.5° daily average can be considered to represent the general feature of the statistics. Another interesting point is that the magnitude of the correlation slope between $\log_{10}N_a$ and $\log_{10}\tau_c$ is greater than that of the correlation between $\log_{10}N_a$ and $\log_{10}r_e$, as also summarized in Table 1, which means the increase of the liquid water path according to equation (8).

[16] Using the r_e and τ_c data sets, the liquid water path and the cloud droplet number concentration are estimated using equations (3) and (4), and the correlation of these parameters with the column aerosol number concentration are calculated. We use the 2.5° × 2.5° daily data to make the correlation plot, because 2.5° × 2.5° daily averaging can produce representative statistics as found from Figures 2 and 5. Figure 6a shows that the liquid water path is almost independent of the aerosol number supporting the result of *Nakajima et al.* [2001]. However, it is worthwhile to find a weak positive correlation of about 10% change for one order of change of the aerosol number, which is consistent with the larger correlation slope of τ_c than that of r_e as also pointed out in Figure 4 and Table 1.

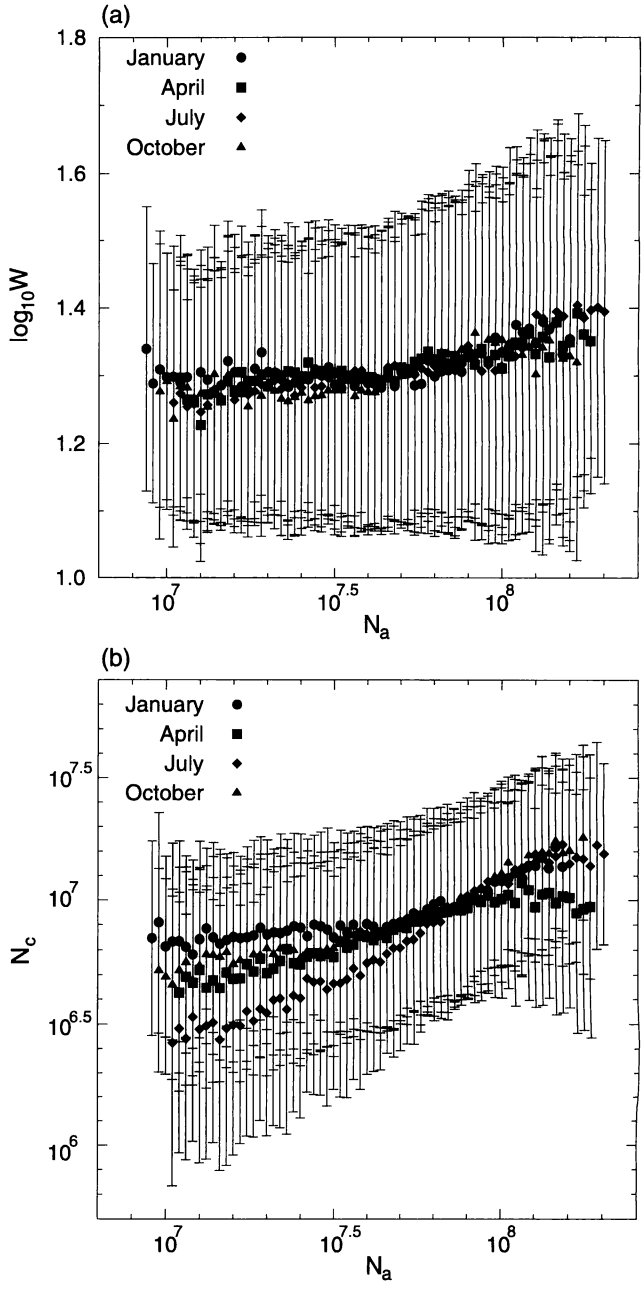

Figure 6. Same as Figure 1, but for the correlation of (a) the liquid water path and (b) the cloud droplet number concentration with the column aerosol number concentration.

Table 2. Correlation Slope Between $\log_{10}N_a$ and $\log_{10}N_c$

Study	Slope	Method
Kaufman et al. [1991]	0.7	aircraft
Leaitch et al. [1992]	0.257	aircraft
Boucher and Lohmann [1995][a]	0.41	model
Lohmann et al. [2000][a,b]	0.48	model
Nakajima et al. [2001][b]	0.50	satellite
Present study[a]	0.388	satellite

[a]Considered to be that of sulfate aerosols.
[b]Considered only over the ocean.

[17] In Figure 6b, we find a linear tendency between the aerosol number concentration ($\log_{10}N_a$) and cloud droplet number concentration ($\log_{10}N_c$). A t test shows that the positive correlation is statistically significant at the 95% significance level. The slope value is around 0.43 ± 0.20, which is similar to those in the past studies from aircraft and satellite measurements as summarized in Table 2.

[18] Changes in the cloud dynamic parameters, i.e., cloud-top temperature, cloud amount and cloud geometrical thickness are also important quantities for estimating the indirect cloud radiative forcing. Figure 7a shows the correlation between $\log_{10}N_a$ and the cloud fraction n. There is a clear positive relationship, which can be considered as a result of the cloud lifetime effect or secondary effect, except for the area of extremely high aerosol loading where there is a tendency of a weak or negative correlation. One reason for the latter phenomenon is that aerosols are accumulated in the clear sky under a persistent high-pressure system. In this situation the semidirect effect [*Hansen et al.*, 1997] of absorbing aerosols can also reduce the cloud amount by evaporating cloud particles. We further investigate the statistics of the cloud geometric thickness as shown in Figure 7b. The cloud geometric thickness is assumed as the difference between the cloud-top height and lifting condensation level. The latter level is calculated from the ECMWF reanalysis data. The figure suggests that the geometric thickness also does not have a significant dependence on the aerosol number on a global scale. Different from the case of the cloud fraction, Figure 8a shows no definite correlation between $\log_{10}N_a$ and T_c with a negative correlation in January and a positive correlation in July. Although *Pincus and Baker* [1994] found a negative correlation, their correlation strength is small (about 1 degree cloud-top temperature change) and cannot be said that their finding is inconsistent with our result of insensitiveness of cloud-top temperature to CCN loading. In order to study this issue in more detail, we classify the atmosphere according to the index of the static stability proposed by *Klein and Hartmann* [1993]

$$\Delta\theta = \theta(P = 700\text{hPa}) - \theta(P_g, T_g), \tag{11}$$

where P_g and T_g are the sea level pressure and surface air temperature using ECMWF reanalysis data sets, respectively. Figure 8b shows the result for the region of $\Delta\theta \geq 15$, where low stratiform clouds are frequently observed. A negative correlation appears in the figure suggesting a stable atmosphere is needed for the phenomenon found by *Pincus and Baker* [1994]. Nonetheless, the correlation is weak supporting our conclusion regarding Figure 8a.

3.2. Regional Correlation Between Aerosol and Cloud Parameters

[19] In this subsection, we investigate the regional correlation between the column aerosol number concentration and cloud parameters in order to find regional differences. We gather $0.5° \times 0.5°$ daily data for a larger sampling area, such as each $2.5° \times 2.5°$ area of the globe, and calculate the slope of the regression line in each sampling area for each month. Similar to the former subsection, we bin the aver-

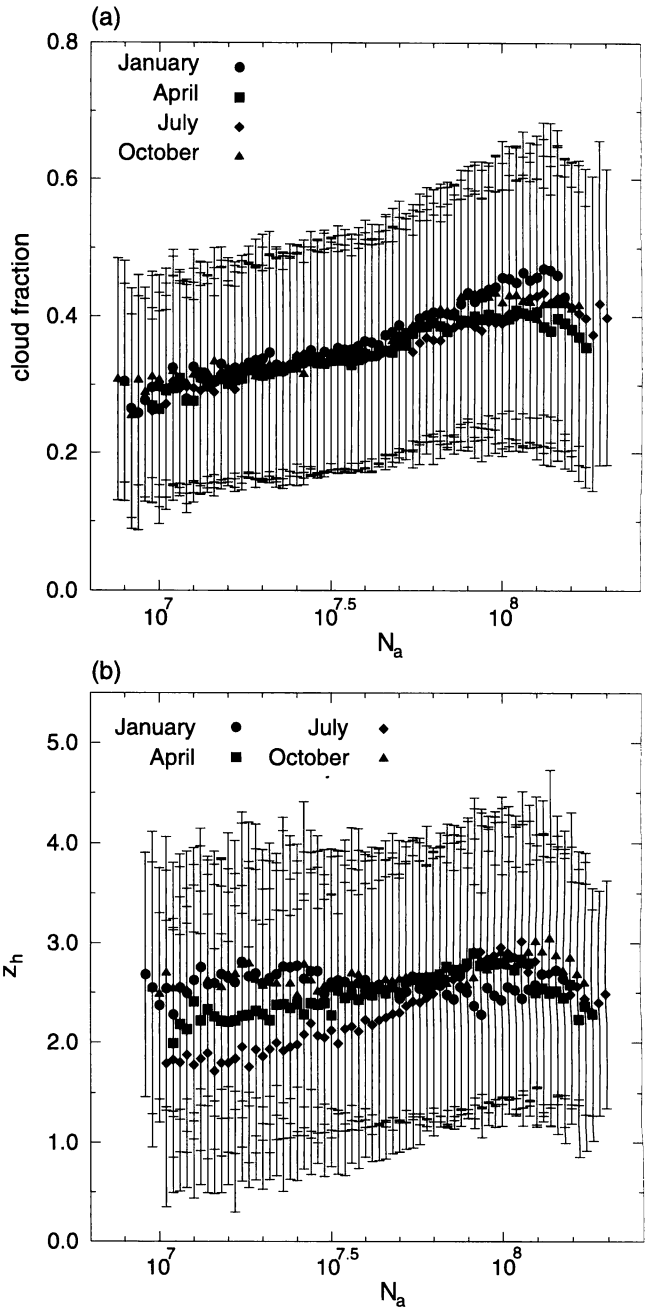

Figure 7. Same as Figure 1, but for the correlation of (a) all cloud fraction and (b) cloud geometrical thickness with the column aerosol number concentration.

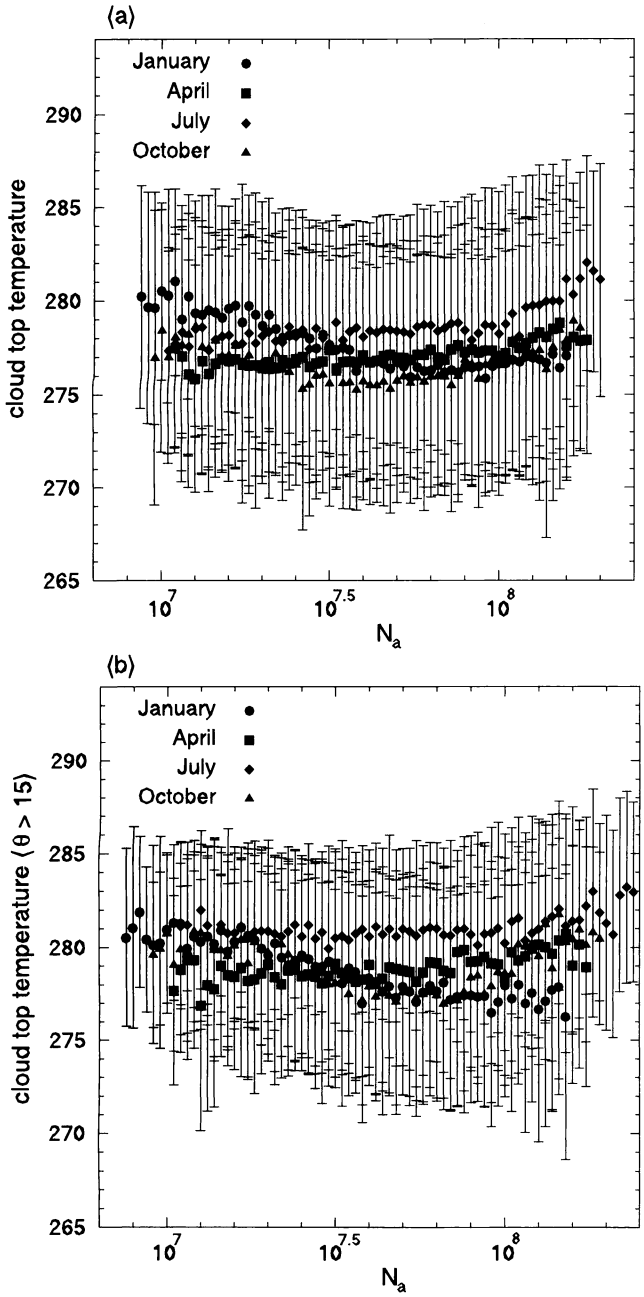

Figure 8. Correlation plots between (a) column aerosol number concentration and cloud-top temperature and (b) plots for the region with $\Delta\theta \geq 15$.

aged data into number bins of $\Delta\log_{10}N_a = 0.02$ to calculate the mean and standard deviation. We do not calculate the correlation in regions that have less than 10 data points. We try several area sizes from 2.5° × 2.5° to 27.5° × 27.5° to see the effect of the sampling area size. Figure 9a shows the correlation slope between $\log_{10}N_a$ and $\log_{10}r_e$ for which we use the AVHRR data with a 17.5° × 17.5° area sampling. The figures (top to bottom) are for January, April, July and October in 1990. Forty percent of the area has a significant negative correlation with a 95% significant level using the *t* test. Negative correlation slopes similar to the global statistics are found along coastal regions of the continents where aerosols of continental origin meet with the clear oceanic air mass, suggesting that the aerosol indirect effect is the dominant cause of the negative correlation. Another important fact in the figure is the correlation slope has a large dependence on the location and time. The correlation is generally not strong in the winter season. Some area, like the Atlantic Ocean, has a distinct seasonal change in the slope even with a positive correlation in the spring season. Also some areas, such as the southern Pacific Ocean, have a positive slope throughout the year.

[20] We take a similar correlation with the three-month POLDER data with a 17.5° × 17.5° area sampling as shown in Figure 9b. Similarly to the AVHRR case, a strong negative correlation is found in most of the coastal zones around continents. It is interesting to find significantly large positive correlation slopes in most land area of China and Canada in the DJF season, and Amazon and India to the Middle East regions in the MAM season. It is difficult to explain such positive correlations only with the first and second indirect effects of aerosols. More comprehensive studies with detailed meso-scale models are needed to understand this phenomenon.

[21] The correlations of the cloud optical thickness, cloud-top temperature and cloud fraction ($\log_{10}\tau_c$, n and T_c) vs. the aerosol column number concentration ($\log_{10}N_a$) are shown in Figures 10a, 10b, and 10c, respectively. Figure 10a shows that most regions have a positive correlation. The 70% area over the globe has correlation with a 95% significance level. The figure indicates that regions with large positive slopes correspond to the regions of significant negative slopes of the effective radius, supporting the indirect effect of aerosols being dominant along the coastal regions around the continent. It is interesting to find that the winter hemisphere tends to have a larger slope in the optical thickness. This phenomenon strongly suggests that an aerosol input to a clear air mass tends to cause a greater second indirect effect to enhance the optical thickness increase. In addition, the atmospheric stability is considered to be concerned in the phenomenon. The continental air tends to be colder than sea surface in the winter season to form a stable atmospheric condition in which the continental aerosols are effectively fed to the marine boundary layer clouds at the coastal regions. This strong physical linkage between the continental aerosols and the low level clouds in the winter season can cause a relatively larger slope and higher correlation than in the summer season. This mechanism can work more effectively near the coastal region than in the offshore region because the air in the marine boundary layer is quickly cleansed by wet deposition induced by seeding effect of sea salt aerosols [*Rosenfeld et al.*, 2002]. The correlation slope of the cloud fraction (Figure 10b) also has features similar to those of the optical thickness. There are some negative areas around the west coast of the Saharan desert and stronger correlations can be seen in the winter hemisphere. Seventy-seven percent of the area has a correlation with a 95% significance level. To our knowledge, there is no other report showing an observed global-scale change in the cloud fraction as a function of CCN loading. However, Figure 10c indicates that the correlation slope of the cloud-top temperature becomes positive and negative depending on the location and season. The clear difference in sign can be seen between the

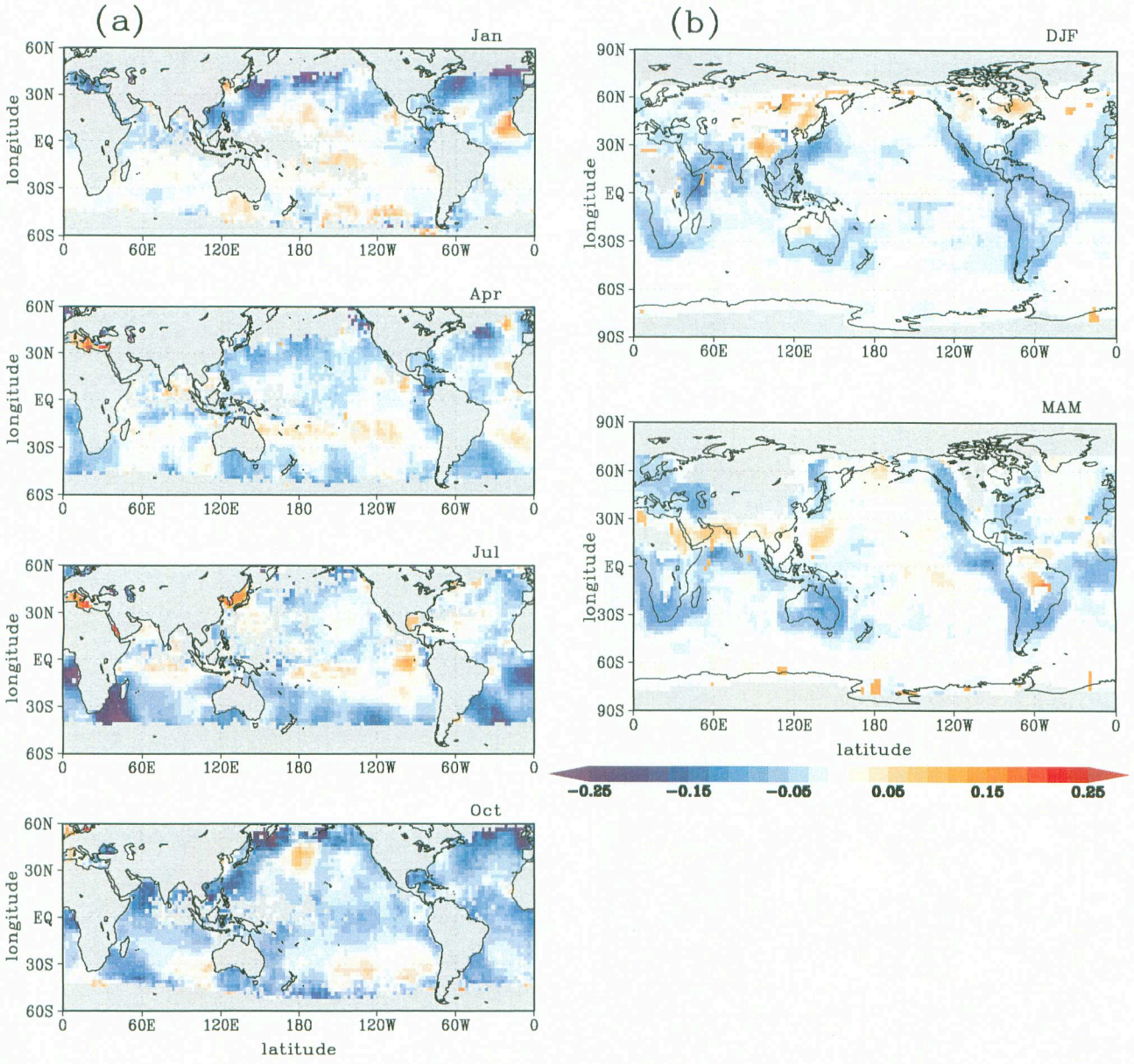

Figure 9. Distributions of the correlation slope between $\log_{10}N_a$ and $\log_{10}r_e$ with (a) AVHRR and (b) POLDER data for 17.5° × 17.5° area sampling.

northern and southern hemispheres in January and October. It is thus concluded that our regional data analysis does not also support a significant common tendency between aerosol and cloud-top temperature.

[22] Figure 11 shows the global averages of the correlation slope and correlation coefficient of τ_c and n with $\log_{10}N_a$ as a function of the sampling area size. It is found that as the area size increases, the correlation slope converges at a fixed value, and the correlation becomes better. Compared with the result of the global sampling method in Figures 2 and 5, the slope of the global correlation thus obtained is larger for τ_c and smaller for n. It is thus concluded that the correlation slope depends on the method of comparison between the cloud parameters and the aerosol number, although the sign of the correlation slope does not depend on the correlation method. We summarize the global averages of the correlation slopes thus obtained in Table 1. As a conclusion, we recommend the sampling method for obtaining the global and regional correlation statistics to be daily and large sampling area, such as 2.5° × 2.5° area averaging. However, too large a sampling area is also not suitable because we lose the validity of taking the correlation between the averages over such a large sampling area.

3.3. Cloud-Top Temperature Change

[23] In the previous section, it was difficult to find a correlation between aerosol and cloud-top temperature, suggesting that the cloud-top temperature is mainly controlled not by the aerosol number, but by dynamic circulation. It should be noted in this regard that *Rosenfeld* [2000] observed that the particles of polluted clouds grow to the precipitation threshold radius of 14 μm [*Rosenfeld and*

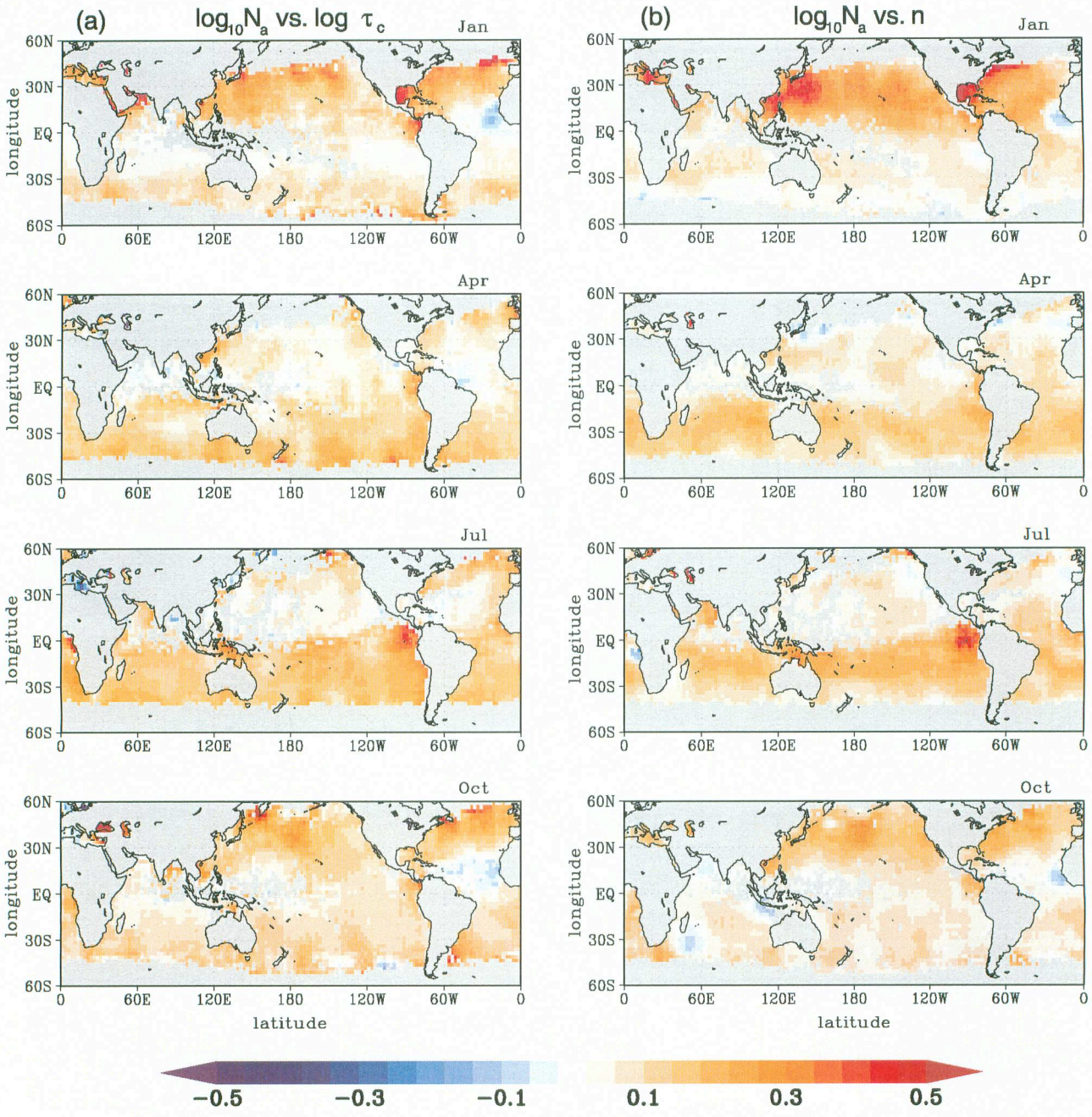

Figure 10. Correlation slopes of (a) $\log_{10}\tau_c$, (b) T_c, and (c) n with $\log_{10}N_a$ for 17.5° × 17.5° area sampling.

Gutman, 1994] slower than that of clean clouds leading to a suppressed precipitation. This observation suggests that the cloud height at which the cloud particles grow to $r_e = 14$ μm is expected to be higher than that in the preindustrial era. In order to investigate this effect on a global scale, we calculate the global distribution of the temperature that cloud particles grow to 14 μm in radius. Hereafter we call this temperature "T_{14}". To obtain T_{14}, the daily 0.5° × 0.5° r_e and T_c are gathered for each month and 2.5° × 2.5° area of the globe and averaged r_e are plotted for each 1K intervals following the method of *Rosenfeld and Lenskey* [1998]. Figure 12 shows the profiles of r_e and T_c in the Amazon and China. The lower the cloud-top temperature, the larger the cloud droplets grow in the Amazon (solid line in Figure 12). In China (broken line in Figure 12), the same tendency is seen in the profile of July, but cloud particles do not appear to grow in January. This result shows that summer pollution significantly suppresses the growth of cloud particles. Using this plot, we evaluate the temperature at T_{14} unless the gradient of the curve is negative or the effective radius does not grow to 14 μm before the temperature is under 258 K. Figure 13 shows the distribution of T_{14}. It is found from the figure that T_{14} is low over and around land, especially the Californian offshore and the east coast of China, where aerosol outflows are frequently observed [*Higurashi et al.*, 2000]. A distinct seasonal

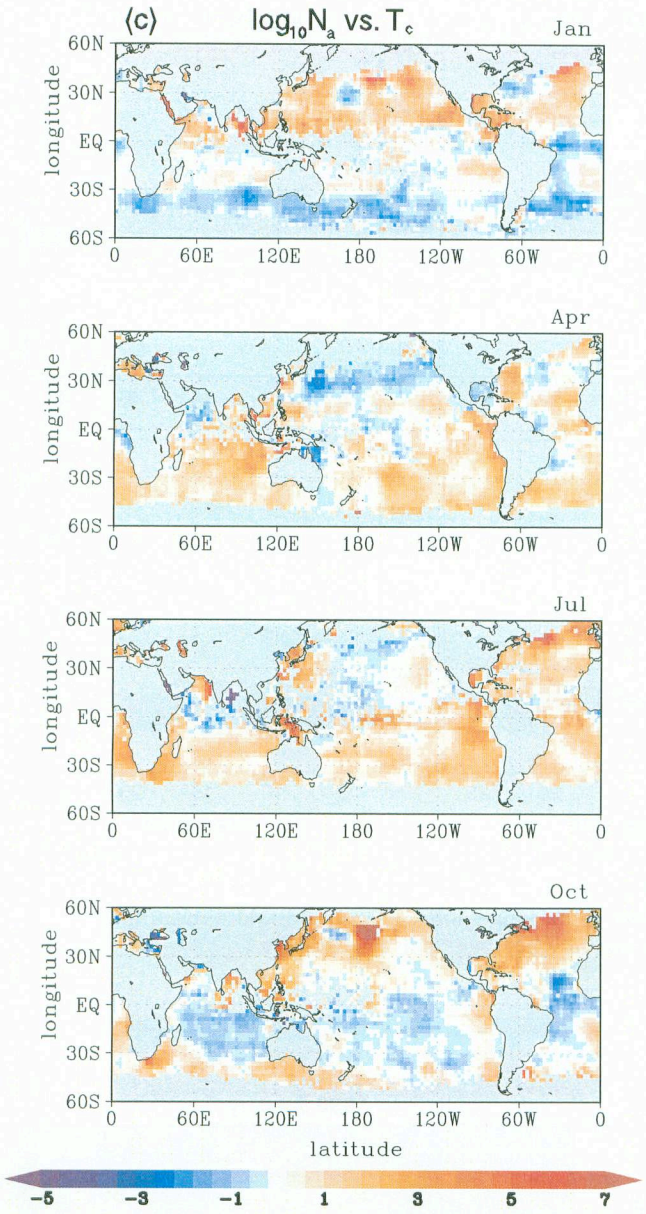

Figure 10. (continued)

change in T_{14} is seen over the Amazon area. There is also a low T_{14} area around the latitude of 20° in the winter hemisphere.

[24] Figure 14 shows the correlation of T_{14} versus $\log_{10}N_a$. Although the correlation coefficient is small in April, the graph for $\log_{10}N_a > 7.8$ has a clear negative slope. Therefore it is concluded that the proposal of *Rosenfeld* [2000] for particle growth suppression of cumulus clouds is also significant for high aerosol concentration cases on a global scale. A t test confirms the existence of a negative correlation with the significant level of 95%.

4. Estimation of the Radiative Forcing

[25] In this section, we evaluate the radiative forcing of the aerosol indirect effect assuming that the cloud parameters have changed along the correlation curves obtained in the preceding sections. We further assume that the globally averaged aerosol number concentration has increased by 30% from the preindustrial era based on the two estimates, i.e., 15% by *Charlson et al.* [1992] and 40% by *Penner et al.* [1999], for deriving the cloud parameters in the preindustrial era. The indirect forcing is then calculated as the difference between the cloud radiative forcing in the present condition and that in the preindustrial condition.

[26] For our first estimation of the indirect forcing, we assume that the cloud effective radius and optical thickness in each region have changed along the global correlation slope using the 2.5° × 2.5° daily data for each month as given in section 3.1. This assumption allows us to estimate the global changes in r_e and τ_c after the industrial revolution as −2.74% and 4.28%, respectively, and calculate the global annual mean radiative forcing as -0.91 ± 0.27 W m^{-2} as shown in Table 3. The first indirect forcing using the assumption that LWC is constant, i.e., the slope of $\log_{10}\tau_c$ is the opposite sign of that of $\log_{10}r_e$, is estimated to be -0.64 ± 0.16 W m^{-2}. This assumption can also be adopted for the POLDER data to obtain the first indirect radiative forcing as -0.37 ± 0.09 W m^{-2} over the ocean. In this regard, it should be noted that *Nakajima et al.* [2001] have found a positive correlation between τ_c and N_a only when $\log_{10}N_a \geq 7.8$. Therefore we try an alternative estimation of the radiative forcing using the regression lines of τ_c and N_a only when $\log_{10}N_a \geq 7.8$. The global mean value of the indirect radiative forcing thus obtained is -0.13 ± 0.05 W m^{-2} (Table 3), which is less than half of the value without the lower limit of N_a in the evaluation. We have to study in the future the statistics of the cloud optical thickness more precisely in order to overcome this ambiguity about the lower limit of the aerosol number used in the analysis, although we have a feeling that the unlimited case is more plausible.

[27] In order to study the uncertainty in the forcing evaluation due to the selection of the cloud correlation slope, our second forcing evaluation is done with the regional correlation slope of the cloud effective radius and optical thickness for each month given in section 3.2. The atmospheric conditions are the same as those of the first estimation using the slope of the global correlation. Figure 15 shows the distribution of the first and second indirect forcings evaluated from data with the 17.5° × 17.5° area sampling. Most areas have a cooling effect except for the west coast of the Saharan desert with a slightly positive forcing. The areas adjacent to the Saharan desert is under an extremely dry condition in which the cloud formation process is much different from those in the other areas. This positive forcing is not significant to the global estimation of the radiative forcing because of the small cloud fraction in this area. The annual global forcing is then calculated to be -0.68 ± 0.16 W m^{-2}, which is somewhat smaller than the indirect forcing using the slope of the global correlation. The first indirect radiative forcings are estimated as -0.16 ± 0.08 (AVHRR) and -0.10 ± 0.06 W m^{-2} (POLDER), which are also smaller than that using the slope of the global correlation.

[28] So far we took into account only the change in the optical thickness and effective particle radius fixing the cloud fraction. If we use the slope of the global correlation between n and $\log_{10}N_a$, the cloud radiative forcing caused by the cloud fraction change after the industrial revolution is

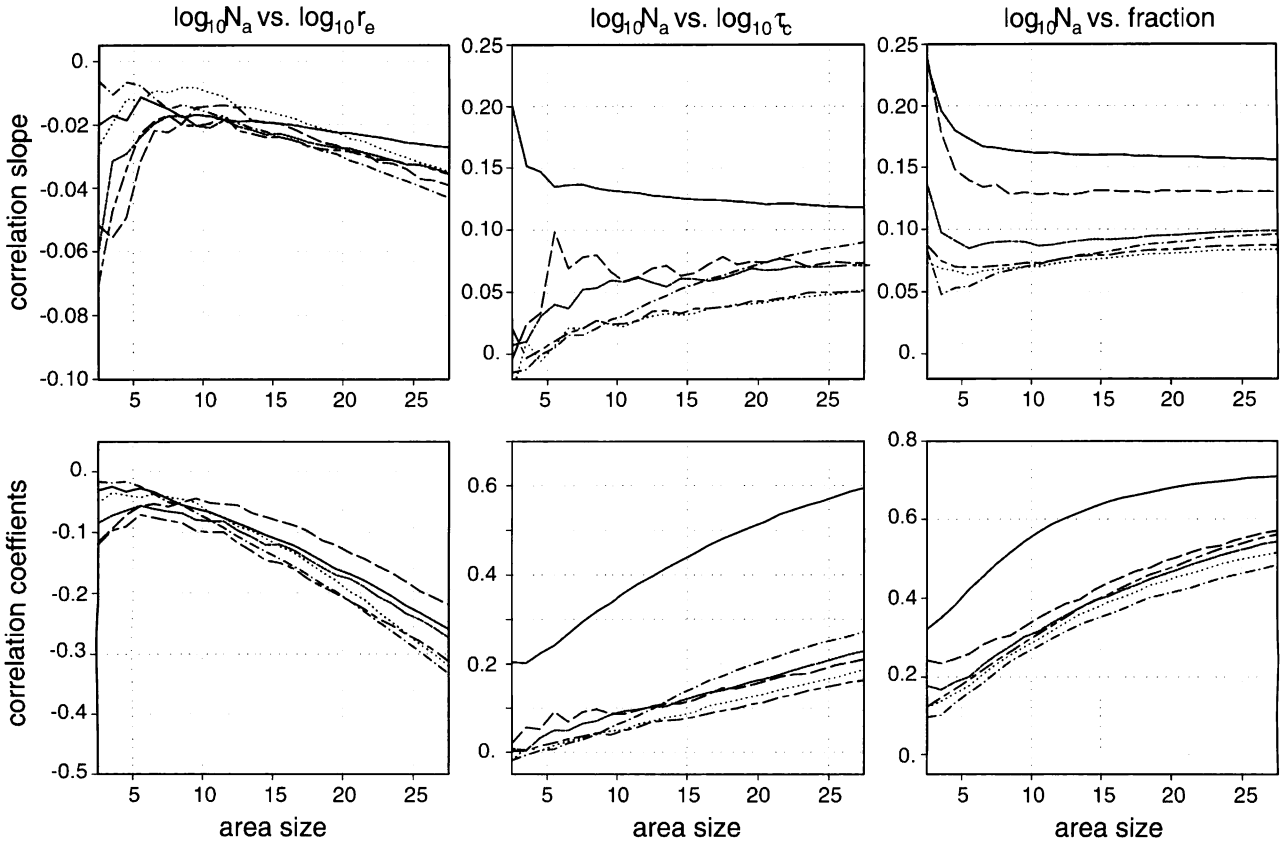

Figure 11. The correlation slope and correlation coefficients of r_e, τ_c and n with $\log_{10}N_a$ as a function of the sampling area size in January. Solid, long dash, short dash, long-short dash, dots, and dot-dash line indicate daily, 3 days, 1 week, 10 days, 2 weeks, and monthly average data, respectively.

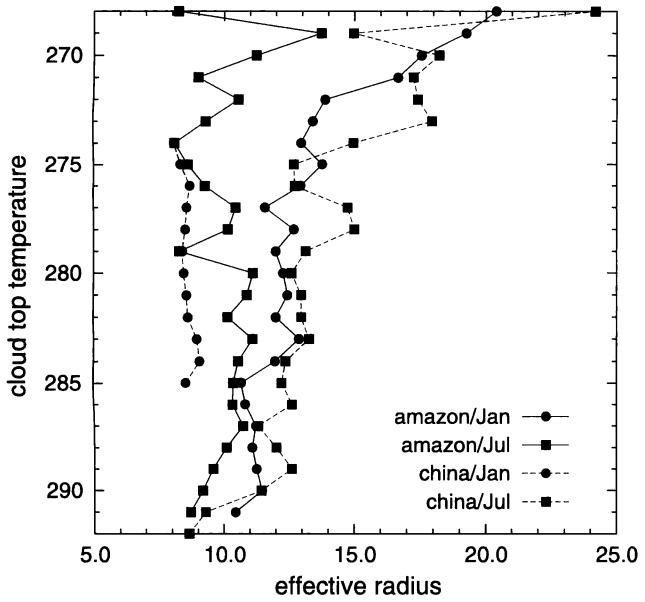

Figure 12. The profiles of r_e vs. T_c in Amazon (solid line) and China (broken line) for each 2.5° × 2.5° area using the daily 0.5° × 0.5° data. Circles and squares indicate January and July 1990, respectively.

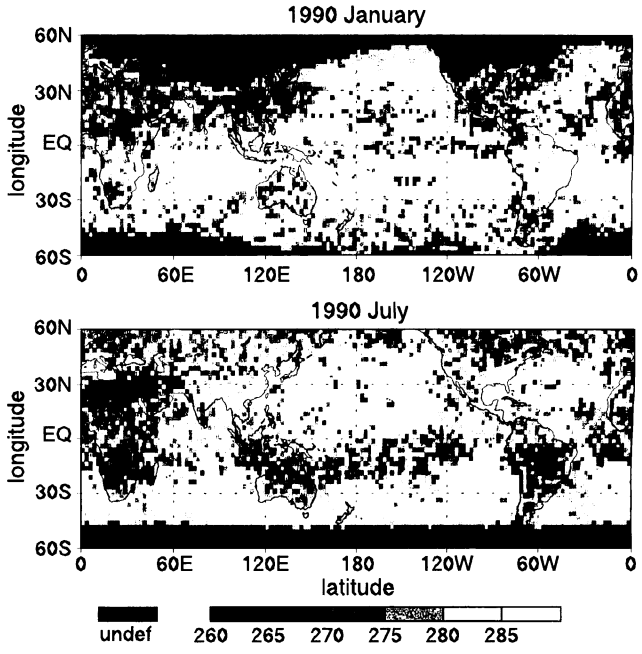

Figure 13. Global distributions of T_{14}. (top) January 1990. (bottom) July 1990.

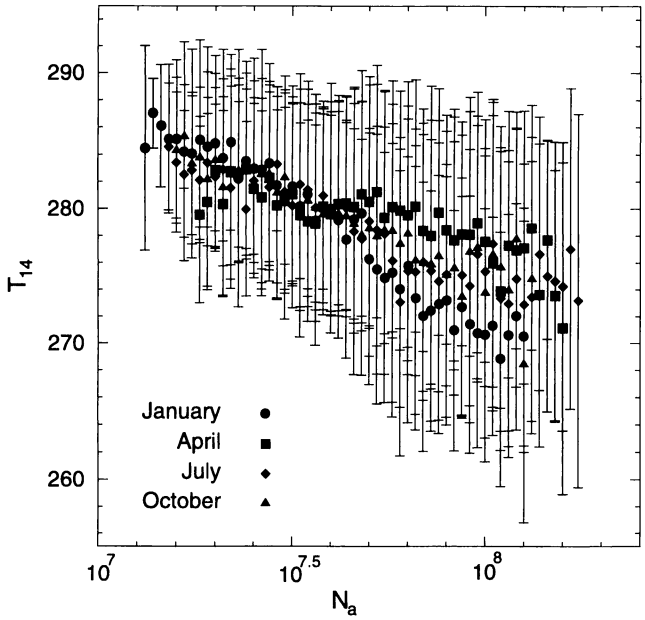

Figure 14. Same as Figure 1, but for the correlation between the column aerosol number concentration and T_{14}.

estimated as -0.54 ± 0.20 W m^{-2}. The annual global average is estimated as -0.73 ± 0.21 W m^{-2} if the regional correlation slope is used. We finally calculate the total forcing with all the indirect effects, i.e., cloud effective radius, optical thickness and cloud fraction, as -1.43 ± 0.43 W m^{-2} (global correlation) and -1.40 ± 0.35 W m^{-2} (regional correlation). These results indicate that the change in the cloud fraction had a substantial cooling effect comparable to the other indirect effects.

[29] It is more difficult to evaluate the effect of the cloud-top temperature change. According to the tendency shown in Figure 1f, the cloud-top temperature did not significantly change. In this case there is no radiative forcing caused by a change in the cloud-top temperature. This may be the most possible scenario of the temperature change. However, the maximum possible forcing can be given by the forcing estimated by supposing that the cloud-top temperature has changed according to the correlation similar to that of T_{14}. In this case, it is found that the cloud-top temperature change is thought to cause a positive forcing of about $+0.87 \pm 0.37$ W m^{-2} to largely reduce the total negative indirect forcing caused by the indirect effects associated with changes in τ_c, r_e, and n. Since there is no resemblance of the correlation for T_c versus $\log_{10}N_a$ to that for T_{14} versus $\log_{10}N_a$, we feel the former scenario without large dependence of the cloud-top temperature on the aerosol number is more possible than the latter for the evaluation of the past change in the radiative forcing after the industrial revolution.

[30] For reference, we also calculated the radiative forcing of the direct effect by simply assuming a 30% increase in the aerosol number all over the globe and that the optical properties are the same as used in the satellite retrieval. The direct radiative forcing is thus estimated to be about -0.40 W m^{-2} over the ocean. It suggests that the direct effect is smaller than the indirect radiative forcing.

5. Discussion and Conclusions

[31] In this study, we found systematic global correlations of the cloud microphysical parameters with the column aerosol number from AVHRR and POLDER remote sensing data. The effective radius has a negative correlation with the aerosol number and the correlation slope does not

Table 3. Annual Mean Values of the Radiative Forcings, W m^{-2}

	AVHRR		POLDER	
	Δ, %	RF	Δ, %	RF
		Global		
First				
Maritime	$\Delta r_e = -2.59$	-0.64 ± 0.16	$\Delta r_e = -1.76$	-0.37 ± 0.09
Continental			$\Delta r_e = -0.98$	-0.04 ± 0.21
First and second				
	$\Delta r_e = -2.59$			
	$\Delta \tau_c = 4.01$	-0.91 ± 0.27		
First and second, $\log_{10}N_a > 7.8$				
	$\Delta r_e = -0.53$			
	$\Delta \tau_c = 0.81$	-0.13 ± 0.05		
Cloud fraction				
	$\Delta n = 0.98$	-0.54 ± 0.20		
Total				
		-1.43 ± 0.43		
T_c	$\Delta T_c = -1.36$ [K]	0.87 ± 0.37		
		Regional		
First				
Maritime	$\Delta r_e = -0.81$	-0.16 ± 0.08	$\Delta r_e = -0.25$	-0.10 ± 0.06
Continental			$\Delta r_e = -1.29$	-0.24 ± 0.08
First and second				
	$\Delta r_e = -0.81$			
	$\Delta \tau_c = 3.20$	-0.68 ± 0.16		
First and second, $\log_{10}N_a > 7.8$				
		-0.12 ± 0.04		
Cloud fraction				
	$\Delta n = 1.31$	-0.73 ± 0.21		
Total				
		-1.40 ± 0.35		

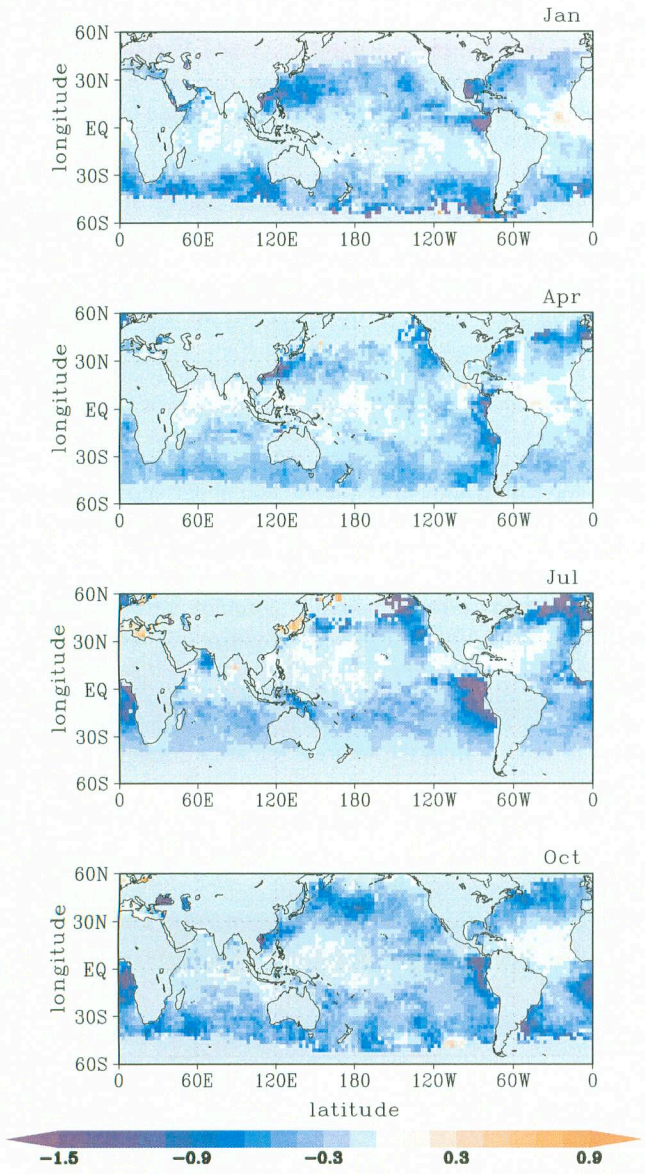

Figure 15. Global distributions of the first and second radiative forcings using regional correlation with 17.5° × 17.5° area sampling.

change much with the sampling method if we adopt the 2.5° × 2.5° area sampling. However, the cloud optical thickness and cloud fraction have a positive correlation with the aerosol number. Both the AVHRR and POLDER data showed a strong negative correlation around the coast zone of the continents. One of topics is the effect of the threshold of cloud-top temperature we used in this study. We tested the condition of $T_c > 273$ K, which is the same assumption as that of *Nakajima et al.* [2001], instead of $T_c > 257$ K used in the present study. We found that the differences between the two results was larger in the monthly sampling method than in the daily one, but not significant enough to change the conclusion presented in the preceding sections, nor can it explain the difference from that of *Nakajima et al.* [2001]. It is, therefore, concluded that the differences between the present result and that of *Nakajima et al.* [2001] are mainly caused by the difference in the sampling methods and the lower limit of the aerosol number used in the analysis.

[32] Using these correlation slopes and the assumption that the aerosol column number concentration have increased by 30% from the preindustrial era, the total radiative forcing of the aerosol indirect effect was then evaluated to be about −0.6 to −1.2 W m^{-2}. This value is somewhat smaller in magnitude than −1.4 W m^{-2} by *Nakajima et al.* [2001] over ocean, but within 0 to −2 W m^{-2} that *IPCC* [2001] indicated. If the indirect effect includes the effect of cloud fraction change, the total indirect radiative forcing is estimated to be about −1.0 to −1.8 W m^{-2}. However, our estimation of the direct forcing is −0.40 W m^{-2} over ocean and is similar to the estimates of −0.42 W m^{-2} by *IPCC* [2001] and −0.2 W m^{-2} by *Takemura et al.* [2002]. These values suggest that the indirect radiative forcing generated after the industrial revolution was greater than the direct forcing, though a large uncertainty still exists in the estimates. The important but uncertain assumption in the indirect effect estimation is the assumption of how much aerosols have increased after the industrial revolution. In our estimation, we assumed a 30% increase, but there are widely varying values given by the past studies ranging from 15% to 100% [*Charlson et al.*, 1992; *Penner et al.*, 1999; T. Takemura, personal communication, 2002]. This wide range of estimates corresponds to the cloud forcing range from −0.3 to −3.0 W m^{-2}. Also, it will not be good to assume the same increase rate of the aerosol number concentration as 30% in all regions for our forcing estimation, because aerosols increased more in urban regions than in the remote ocean area from the preindustrial era. We need more future studies of evaluating the preindustrial values of aerosol and cloud parameters.

[33] The cloud-top temperature did not have a global nor regional correlation with the aerosol number in the present study, because the cloud-top height is mainly determined by the vertical temperature and humidity profiles. In spite of this insignificance of the cloud-top temperature, the cloud temperature at which cloud particles grow to 14 μm in radius, T_{14}, has a clear negative correlation with the aerosol number. If this change occurs in the entire cloud system, the induced radiative forcing is estimated to be about +0.87 W m^{-2}, although we feel this scenario is unlikely as the past change in the cloud-top temeperature. Nonetheless it is not too wrong to conclude that the cloud-top temperature change has the potential to largely suppress the forcing and turn the sign of the forcing to positive. We also should pay attention our finding of the large aerosol effect on T_{14} means substantial effects of suppressing the precipitation by aerosols occurring on a global scale. This is the source of the effect on the cloud lifetime and cloud cover, which was found here to be greater than the direct radiative effect. Furthermore, it is possible in the real situation of increasing aerosols that anthropogenic aerosol increase changes the cloud-top temperature and humidity profiles by the induced secondary circulation, and thus change the cloud-top temperature [*Santer et al.*, 1996]. This effect is not separated from other effects in our statistical analysis that is based on the cloud field changes caused by the regional aerosol concentration change. In summary, we still need for future studies to improve the present estimates for the radiative forcing of the indirect

aerosol effects, after solving several difficulties observed in the present investigation.

[34] **Acknowledgments.** This work was supported by JST/CREST/Asian Atmospheric Particle Environmental Change Studies (APEX) project. The authors are grateful to M. Yasumoto of Kinki University for providing us with retrieved POLDER data and S. Katagiri of NASDA for AVHRR segmented data processing. We also thank R. Furue and I. Ishii for computing support in CCSR.

References

Ackerman, A. S., O. B. Toon, D. E. Stevens, A. J. Heymsfield, V. Ramanathan, and E. J. Welton, Reduction of tropical cloudiness by soot, *Science*, *288*, 1042–1047, 2000.

Albrecht, B. A., Aerosols, cloud microphysics and fractional cloudiness, *Science*, *245*, 1227–1230, 1989.

Boucher, O., and U. Lohmann, The sulfate-CCN-cloud albedo effect: A sensitivity study with two general circulation models, *Tellus, Ser. B*, *47*, 281–300, 1995.

Charlson, R. J., S. E. Schwartz, J. M. Hales, R. D. Cess, J. A. Coakley Jr., J. E. Hansen, and D. J. Hofmann, Climate forcing by anthropogenic, *Science*, *255*, 423–430, 1992.

Han, Q., W. B. Rossow, J. Chou, and R. M. Welch, Global survey of the relationship of cloud albedo and liquid water path with droplet size using ISCCP, *J. Clim.*, *11*, 1516–1528, 1998.

Hansen, J., M. Sato, and R. Ruedy, Radiative forcing and climate response, *J. Geophys. Res.*, *102*, 6831–6864, 1997.

Higurashi, A., and T. Nakajima, Development of a two-channel aerosol algorithm on global scale using NOAA AVHRR, *J. Atmos. Sci.*, *56*, 924–941, 1999.

Higurashi, A., T. Nakajima, B. N. Holben, A. Smirnov, R. Frouin, and B. Chatenet, A study of global aerosol optical climatology with two-channel AVHRR remote sensing, *J. Clim.*, *13*, 2011–2027, 2000.

Intergovernmental Panel on Climate Change (IPCC), *Climate Change 2001: The Scientific Basis*, edited by J. H. Houghton et al., 881 pp., Cambridge Univ. Press, New York, 2001.

Jones, A., and A. Slingo, Predicting cloud-droplet effective radius and indirect sulphate aerosol forcing using a general circulation model, *Q. J. R. Meteorol. Soc.*, *122*, 1573–1595, 1996.

Jones, D., D. L. Robarts, and A. Slingo, A climate model study of indirect radiative forcing by anthropogenic sulphate aerosols, *Nature*, *370*, 450–453, 1994.

Kaufman, Y. J., and R. S. Fraser, Control of the effect of smoke particles on clouds and climate by water vapor, *Science*, *277*, 1636–1639, 1997.

Kaufman, Y. J., and T. Nakajima, Effect of Amazon smoke on cloud microphysics and albedo-Analysis from satellite imagery, *J. Appl. Meteorol.*, *32*, 729–744, 1993.

Kaufman, Y. J., R. S. Fraser, and R. L. Mahoney, Fossil fuel and biomass burning effect on climate-Heating or cooling?, *J. Clim.*, *4*, 578–588, 1991.

Kawamoto, K., T. Nakajima, and T. Y. Nakajima, A global determination of cloud microphysics with AVHRR remote sensing, *J. Clim.*, *14*, 2054–2068, 2001.

Klein, S. A., and D. L. Hartmann, The seasonal cycle of low stratiform clouds, *J. Clim.*, *6*, 1587–1606, 1993.

Leaitch, W. R., G. A. Isaac, J. W. Strapp, C. M. Banic, and H. A. Wiebe, The relationship between cloud droplet number concentrations and anthropogenic pollution: Observation and climatic implications, *J. Geophys. Res.*, *97*, 2463–2474, 1992.

Lohmann, U., and J. Feichter, Impact of sulfate aerosols on albedo and lifetime of clouds: A sensitivity study with the ECHAM4 GCM, *J. Geophys. Res.*, *102*, 13,685–13,700, 1997.

Lohmann, U., J. Feichter, J. Penner, and R. Leaitch, Indirect effect of sulfate and carbonacerous aerosols: A mechanistic treatment, *J. Geophys. Res.*, *105*, 12,193–12,206, 2000.

Martin, G. M., D. W. Johnson, and A. Spice, The measurement and parameterization of effective radius of droplets in warm stratocumulus clouds, *J. Atmos. Sci.*, *51*, 1823–1842, 1994.

Mukai, S., and I. Sano, Retrieval algorithm for atmospheric aerosols based on multi-angle viewing of ADEOS/POLDER, *Earth Planets Space*, *51*, 1247–1254, 1999.

Nakajima, T., and T. Nakajima, Wide-area determination of cloud microphysical properties from NOAA AVHRR measurements for FIRE and ASTEX regions, *J. Atmos. Sci.*, *52*, 4043–4059, 1995.

Nakajima, T., M. Tsukamoto, Y. Tsushima, A. Numaguti, and T. Kimura, Modeling of the radiative process in an atmospheric general circulation model, *Appl. Opt.*, *39*, 4869–4878, 2000.

Nakajima, T., A. Higurashi, K. Kawamoto, and J. E. Penner, A study of correlation between satellite-derived cloud and aerosol microphysical parameters, *Geophys. Res. Lett.*, *28*, 1171–1174, 2001.

Penner, J. E., C. C. Chuang, and K. Grant, Climate change and radiative forcing by anthropogenic aerosols: Research findings during the last 5 years, Inst. for Adv. Phys. Stud., La Jolla Int. Sch. of Sci., La Jolla, Calif., 1999.

Pincus, R., and M. B. Baker, Effect of precipitation on the albedo susceptibility of clouds in the marine boundary layer, *Nature*, *372*, 250–252, 1994.

Ramanathan, V., P. J. Crutzen, J. T. Kiehl, and D. Rosenfeld, Aerosol, climate, and the hydrological cycle, *Science*, *294*, 2119–2124, 2001.

Rosenfeld, D., Suppression of rain and snow by urban and industrial air pollution, *Science*, *287*, 1793–1796, 2000.

Rosenfeld, D., and G. Gutman, Retrieving microphysical properties near the tops of potential rain clouds by multispectral analysis of AVHRR data, *J. Atmos. Res.*, *34*, 259–283, 1994.

Rosenfeld, D., and I. M. Lensky, Satellite-based insights into precipitation formation processes in continental and maritime convective clouds, *Bull. Am. Meteorol. Soc.*, *79*, 2457–2476, 1998.

Rosenfeld, D., R. Lahav, A. P. Khain, and M. Pinsky, The role of sea-spray in cleansing air pollution over ocean via cloud processes, *Science*, *297*, 1667–1670, 2002.

Rossow, W. B., and R. A. Schiffer, Advances in understanding clouds from ISCCP, *Bull. Am. Meteorol. Soc.*, *80*, 1–27, 1999.

Sano, I., and S. Mukai, Algorithm description of system flow for global aerosol distribution, *Appl. Math. Comput.*, *116*, 79–91, 2000.

Santer, B. D., et al., A search for human influences on the thermal structure of the atmosphere, *Nature*, *382*, 39–46, 1996.

Takemura, T., T. Nakajima, O. Dubovik, B. N. Holben, and S. Kinne, Single-scattering albedo and radiative forcing of various aerosol species with a global three-dimensional model, *J. Clim.*, *15*, 333–352, 2002.

Twomey, S., Pollution and the planetary albedo, *Atmos. Environ.*, *8*, 1251–1256, 1974.

Twomey, S., An assessment of the impact of pollution on global cloud albedo, *Tellus, Ser. B*, *36*, 356–366, 1984.

Wetzel, M., and L. L. Stowe, Satellite-observed patterns in the relationship of aerosol optical thickness to stratus cloud microphysics and shortwave radiative forcing, *J. Geophys. Res.*, *104*, 31,287–31,299, 1999.

Yasumoto, M., I. Sano, and S. Mukai, Combined use of OCTS and POLDER for cloud retrieval, *Adv. Space Res.*, *29*, 39–44, 2002.

A. Higurashi, National Institutes for Environmental Studies, 16-2 Onogawa, Tsukuba, Ibaraki 305-8506, Japan. (hakiko@nies.go.jp)

K. Kawamoto, Research Institute for Humanity and Nature, 335 Takashima-cho, Marutamachi-dori Kawaramachi nishi-iru, Kamigyo-ku, Kyoto 602-0878, Japan. (kawamoto@chikyu.ac.jp)

S. Mukai and I. Sano, Faculty of Science and Technology, Kinki University, 3-4-1 Kowakae, Higashi-Osaka 577-8502, Japan. (mukai@im.kindai.ac.jp; sano@im.kindai.ac.jp)

T. Nakajima, M. Sekiguchi, and K. Suzuki, Center for Climate System Research, University of Tokyo, 4-6-1 Komaba, Meguto-ku, Tokyo 153-8904, Japan. (teruyuki@ccsr.u-tokyo.ac.jp; miho@ccsr.u-tokyo.ac.jp; kenta@ccsr.u-tokyo.ac.jp)

D. Rosenfeld, Hebrew University of Jerusalem, Givat Ram, Jerusalem 91904, Israel. (daniel@vms.huji.ac.il)